PAPER

How to synthesize pure $Li_{2-x}FeSi_{1-x}P_xO_4$/C (*x* = 0.03–0.15) easily from low-cost Fe^{3+} as cathode materials for Li-ion batteries†

Weihua Chen,*[a] Dan Zhu,[a] Yanyang Li,[a] Chaopeng Li,[a] Xiangming Feng,[a] Xinxin Guan,[a] Changchun Yang,[a] Jianmin Zhang*[a] and Liwei Mi*[b]

Li_2FeSiO_4 is a low-cost, environmentally friendly electrode material with high theoretical capacity. However, obtaining pure-phase Li_2FeSiO_4 on a large scale is difficult. In this study, pure $Li_{2-x}FeSi_{1-x}P_xO_4$/C is prepared easily by using the low cost compound $Fe(NO_3)_3 \cdot 9H_2O$, with the help of citric acid and appropriate ratios of $NH_4H_2PO_4$ (*x* = 0.03–0.15). The possible mechanism of the system with $NH_4H_2PO_4$ to synthesize $Li_{2-x}FeSi_{1-x}P_xO_4$/C is that there is a catalysis process in the system, which helps to produce H_2, providing a reducing environment in every particle of the reactants guaranteeing a complete change from Fe^{3+} to Fe^{2+}. The produced H_2 is verified by the gas chromatography of the collected gas produced in the calcination process. The ratios of $NH_4H_2PO_4$ in this system could adjust the valence of element Fe in the products. Without $NH_4H_2PO_4$, an Fe_2O_3 impurity is formed accompanying the Li_2FeSiO_4. With the addition of 1 at% $NH_4H_2PO_4$, the Li_4SiO_4 impurity accords with the objective $Li_{2-x}FeSi_{1-x}P_xO_4$/C. Also, Fe with zero-valence could be found as an impurity with the addition of 20 at% $NH_4H_2PO_4$ due to overreduction in the system. The synthesized pure $Li_{2-x}FeSi_{1-x}P_xO_4$/C (*x* = 0.03) displayed the highest discharge capacity of 179 mA h g^{-1} in the first cycle, the best discharge capacity retention and the most reliable redox reversibility of the coulombic efficiency (approximately 100%), compared with the synthesized materials with Fe_2O_3 or Li_4SiO_4 impurities.

Introduction

Lithium-ion batteries (LIBs) are the most widely used energy storage devices because of their high energy densities and long life cycles.[1–4] Cathodes with high energy density and a good level of safety are desirable for high-performance LIBs, given that they comprise a substantial part of the cost, weight, and volume of a battery.[5–7] The most common cathode materials in practical application are $LiMO_2$ (M = Co, Mn, Ni, and others) and $LiFePO_4$. $LiMO_2$, such as $LiCoO_2$,[8] $LiNi_{0.8}$-$Co_{0.1}Mn_{0.1}O_2$,[9] $LiNi_{0.8}Co_{0.15}Al_{0.05}O_2$,[10] and $LiNi_{1/3}Co_{1/3}$-$Mn_{1/3}O_2$,[11] have attracted significant interest as cathode materials for rechargeable LIBs since the 1990s because of their high energy density. However, they have the disadvantages of high cost, toxicity, and a limited capability or safety.

In current production, $LiFePO_4$ has a good cycling stability, high thermal stability, low cost, and environmental friendliness as a kind of next-generation cathode material, but its low theoretical discharge capacity (170 mA h g^{-1})[12] seriously limits its application. Hence, an electrode material with desirable overall properties is currently explored.

A new kind of cathode material, Li_2FeSiO_4, has recently elicited increasing attention because of its highly safe, low-cost, environmentally friendly, and high theoretical capacity (332 mA h g^{-1} for 2 Li storage capacity) characteristics.[13–17] In addition, the strong Si–O bonds of Li_2FeSiO_4 promote the same lattice stabilization effect as that of $LiFePO_4$ and maintain their structure during the charge–discharge process, resulting in improved cycling stability of the batteries.[18,19] However, like most polyanion-type cathode materials, Li_2FeSiO_4 suffers from shortcomings of low ionic–electronic conductivity[20] and intrinsic electron conductivity (10^{-9} S cm^{-1} at room temperature),[21,22] which are the main reasons impeding the realization of their high-capacity and good cycling performance. Yang *et al.*[23] prepared a hierarchical porous Li_2FeSiO_4/C grown on interconnected carbon frameworks using an *in situ* template synthesis; the composite demonstrated a very high capacity of 254 mA h g^{-1} at room tempera-

[a]College of Chemistry and Molecular Engineering, Zhengzhou University, Zhengzhou, 450001, P. R. China. E-mail: chenweih@zzu.edu.cn, zhjm@zzu.edu.cn; Fax: +86-371-67781556

[b]Center for Advanced Materials Research, Zhongyuan University of Technology, Zhengzhou, 450007, P.R. China. E-mail: mlwzzu@163.com

ture with excellent cycling stability and rate capability. Mitra et al.[3] synthesized Li_2FeSiO_4/MWCNTs that exhibited a first specific capacity of 240 mA h g^{-1} at an electric current density of 16.5 mA g^{-1}. Zhang et al.[24] mixed graphene with Li_2FeSiO_4 in the preparation process and the specific discharge capacities of the resulting material reach up to 310 mA h g^{-1}, corresponding to 1.86 Li$^+$ ions exchange per Li_2FeSiO_4 molecule. Such high capacity is mainly due to the formation of a carbon framework comprising long carbon chains.[25] In addition, the continuous graphene nanosheets serve as a fast 3D path for electron migration during the charge–discharge processes,[22] thereby enhancing the electrochemical performance, especially at high current densities.

Meanwhile, studies on the mechanisms involved during charge–discharge of this kind of material play an important role on realizing high capacity. Orikasa et al.[26] investigated the relationship between the phase transition process involved in cationic exchange and the charge–discharge rate. The results of synchrotron X-ray diffraction (XRD) measurements show that a higher charge–discharge rate entails less Fe sites movement into vacant Li sites, resulting in lower capacity. Yang et al.[27] studied the electrochemical mechanism of Li_2FeSiO_4 with reversible extraction/insertion of more than one Li$^+$ ion. The results indicate that Li_2FeSiO_4 undergoes a two-step phase-transition process, in which the valence of the Fe ions is increased when the electrode is charged to a high voltage of 4.8 V, and Fe^{3+} and Fe^{4+} are formed above the charging voltages of 3.2 V and 4.1 V, respectively. Armstrong et al.[28] concluded that this structure undergoes a change from the initial γ_s phase to an inverse β_{II} phase in the charge–discharge process, as revealed by computer modeling.

Understanding thoroughly the synthesis process of Li_2FeSiO_4 is another crucial aspect not only for its theoretical investigation but also for large-scale application. Although pure-phase Li_2FeSiO_4 have been obtained by some research groups,[24,29,30] impurities such as Fe$_3$O$_4$,[31–34] LiFeO$_2$,[14] and $Li_2SiO_3$[35–37] remain a concern for other researchers since Nytén et al.[17] introduced Li_2FeSiO_4 as a new LIB cathode material. Incomplete reduction of the Fe(III) precursor or partial oxidation of the Fe(II) precursor during the synthesis process should be mainly responsible for the presence of these impurities. In addition, some researchers obtained Li_2FeSiO_4·LiFePO$_4$/C using NH$_4$H$_2$PO$_4$ as one of the raw materials, because the electrical conductivity of LiFePO$_4$ is higher than Li_2FeSiO_4.[29] Therefore, we here try to use NH$_4$H$_2$PO$_4$ as the P source in the process to obtain the solid solution of Li_2FeSiO_4 and LiFePO$_4$. The composition of the investigated compounds can be represented as $Li_{2-x}FeSi_{1-x}P_xO_4$.

In this work, pure $Li_{2-x}FeSi_{1-x}P_xO_4$/C materials were synthesized easily from the low-cost compound Fe(NO$_3$)$_3$·9H$_2$O by adjusting the amount of NH$_4$H$_2$PO$_4$. Here, NH$_4$H$_2$PO$_4$ is added during the synthesis process as the P source, which also acts as an important substance to control the valence of Fe. In addition, the possible synthesis mechanism is analysed. Moreover, the electrochemistry of the investigated compounds has been measured.

Experimental section

Synthesis

$Li_{2-x}FeSi_{1-x}P_xO_4$/C composites were synthesized via a sol–gel method as shown in Scheme 1. First, polyethylene glycol and nano-sized SiO$_2$ were dispersed in deionized water, followed by ultrasonicating for at least 1 h until a white and transparent solution was obtained. Stoichiometric amounts of LiCH$_3$COO·2H$_2$O, citric acid, Fe(NO$_3$)$_3$·9H$_2$O and different amounts of NH$_4$H$_2$PO$_4$ were then added into the above-mentioned solution while stirring. The mixture was dried at 70 °C until a dry gel was formed, and then mixed with sucrose using ball-milling with acetone as a dispersant for 8 h. The obtained mixture was heated at 650 °C for 7 h with a heating rate of
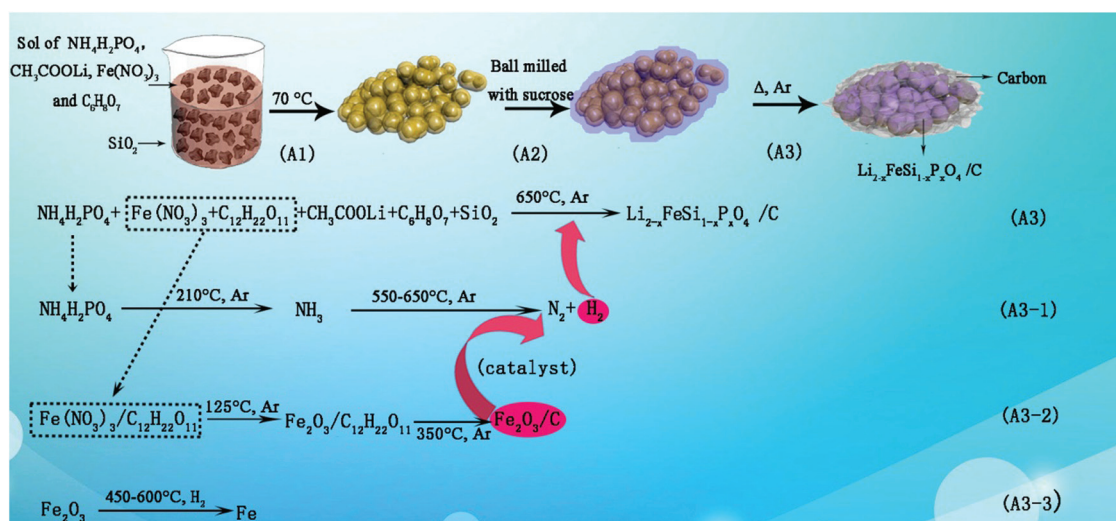
Scheme 1   Illustration of the synthetic procedure of the as-synthesized materials and the synthesis mechanism.

5 °C min⁻¹ at 20–500 °C and 10 °C min⁻¹ at 500–650 °C under high-purity Ar (99.999%). After the temperature was cooled to room temperature, the target material $Li_{2-x}FeSi_{1-x}P_xO_4$/C was obtained.

With the previously-mentioned experimental process, when the molar ratios of $NH_4H_2PO_4$/($NH_4H_2PO_4$ + SiO_2) in the reactants were set as 0%, 1%, 3%, 4%, 8%, 10%, 15% and 20%, respectively, the obtained corresponding samples were labelled as 0LFS, 1LFS, 3LFS, 4LFS, 8LFS, 10LFS, 15LFS and 20LFS, respectively.

Characterization techniques

The gas chromatography tests were performed using a chromatographic working station (Agilent 7890B). The test conditions were set as follows: injector temperature was maintained at 50 °C. N_2 (99.999%) was used as the carrier gas at a flowing rate of 10 mL min⁻¹. The detector is TCD with negative polarity and its temperature is 150 °C, the chromatographic column used in the test is SUPELCO Porapak Q. Injector of 500 µL was used for hand sampling. The injection volumes of pure H_2 (99.999%), pure Ar (99.999%), mixed gas (V_{H_2} : V_{Ar} = 1 : 4) and collected gas produced by the reaction in this work were 100, 500, 500 and 500 µL, respectively. The structures of the synthesized materials were characterized by XRD (Bruker D8 Advance) with a Cu Kα rotating target. The diffraction profile was scanned over the 2θ range of 15° to 80°. Mössbauer spectra were measured in transmission mode at room temperature, together with a calibration spectrum for α-Fe foil. Co was used as a γ-ray source and the spectra were fitted by using Wissel GmbH. ICP emission spectrometry (ICAP6500) was used to determine the contents of metal elements.

A fourier transform infrared (FTIR) spectrometer (Perkin Elmer, USA) and a Bruker IFS 66 V s⁻¹ infrared spectrometer were used to elucidate the chemical structure of materials. Raman spectroscopy (Lab RAM Aramis, Horiba Jobin Yivon) was applied to study the structural properties of carbonaceous materials in the products. A scanning electron microscopy (SEM) system (JSM-7500F) with energy-dispersive X-ray spectroscopy and a transmission electron microscopy (TEM) system (Tecnai G² F20) were used to determine the morphologies and chemical composition. The Brunauer–Emmet–Teller (Tristar II 3020, USA) test was used to identify the surface area of the synthesized materials. The carbon content of the obtained materials was confirmed by elemental analyzer (FLASH EA 1112, Thermo).

Electrochemical measurements

The electrode slices were obtained from the active materials, carbon black, polytetrafluoroethylene (PTFE), and carboxymethyl cellulose at a weight ratio of 85 : 10 : 4 : 1. After drying for at least 12 h at 120 °C in an oven, the electrode slices served as the working electrode, and lithium plates acted as the negative electrode. The average loading amount of the cathode active materials was 8.9 mg cm⁻². The cells (CR2016 coin type) were assembled in an argon-filled glove box using 1 mol L⁻¹ $LiPF_6$ dissolved in ethylene carbonate and dimethyl carbonate (1 : 1, v/v) as the electrolyte. Polypropylene was used as the diaphragm to prevent short circuits while Li⁺ passed through. Charge–discharge tests of the cells were performed using a battery test system (CT2001A LAND) within 1.5 V to 4.8 V under a constant current density of 10 mA g⁻¹. The specific capacities were calculated on the basis of the amount of the active material, excluding the mass of the coated carbon. Cyclic voltammetry (CV) and electrochemical impedance spectroscopy (EIS) were performed on an electrochemical workstation (CHI604E). CV was performed at a scan rate of 0.1 mV s⁻¹ within 1.5 V to 4.8 V, and EIS was conducted at open circuit voltage within the frequency range of 100 kHz to 0.01 Hz. All of the electrochemical measurements were performed at room temperature, and the reported electric potential is relative to Li/Li⁺.

Results and discussion

SEM images of the as-synthesized 0LFS, 1LFS, and 3LFS [Fig. 1(a–c)] show the obvious agglomerate structure of all of the LiFeSiO₄/C materials. The grain size of the agglomerates is approximately 20 nm, which retains a similar morphology to SiO_2 in general [Fig. 1(e)]. Moreover, their loose structures imply large specific surface areas. The N_2 adsorption–desorption isotherms (Fig. 2) indicate that the specific surface areas of 0LFS and 3LFS are 81.7280 and 59.5179 m² g⁻¹,
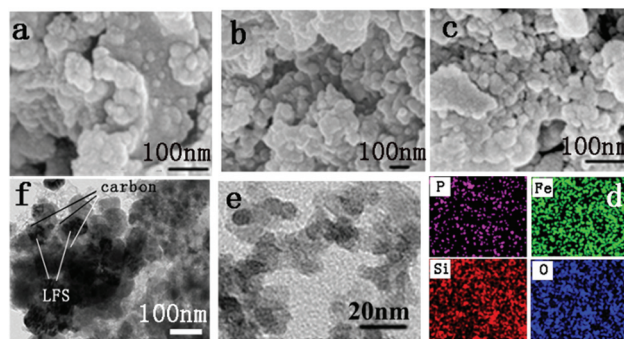

Fig. 1 SEM images of the as-synthesized 0LFS (a), 1LFS (b) and 3LFS (c), elemental mappings of P, Fe, Si and O of 3LFS (d), TEM images of SiO₂ particles (e) and TEM images of 3LFS (f).
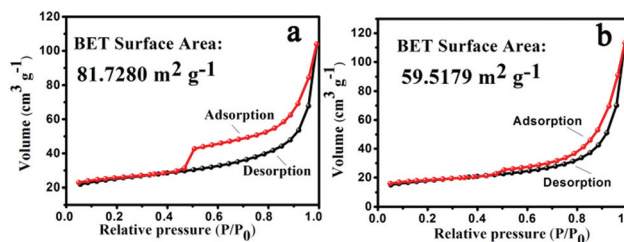

Fig. 2 N₂ adsorption–desorption isotherms at 77 K of as-synthesized 0LFS (a) and 3LFS (b).

respectively. The EDS mapping images of 3LFS (Fig. 1f) show that elemental Fe, Si, and O are obvious and uniform, with low P content, which is consistent with the molecular formula. In addition, the carbon distribution in the obtained material was confirmed *via* TEM. As shown in Fig. 1f, a carbon film is coated on the surface of 3LFS. Large particles of 3LFS can be found clearly because of agglomeration. The carbon content of the as-synthesized materials 0LFS, 1LFS, and 3LFS is 20.49, 22.19, and 20.70 wt%, respectively, which has been confirmed by elemental analysis.

The XRD patterns of the as-synthesized materials $Li_{2-x}FeSi_{1-x}P_xO_4$/C are shown in Fig. 3 and S1.† The XRD patterns of 3LFS in Fig. 3 and 4%, 8%, 10%, 15% in Fig. S1† have similar diffraction peaks, which match well with those of Li_2FeSiO_4 (PDF no. 01-077-4347) without clear diffraction peaks of impurities. The intensity weakens from 3LFS to 15LFS indicating that the crystallinity of the obtained $Li_{2-x}FeSi_{1-x}P_xO_4$/C decreases with the increasing amount of P in the solid solutions. In addition, as reported in the reference, there are at least three different structures for Li_2FeSiO_4, namely the monoclinic (S.G. $P2_1/n$) and orthorhombic (S.G. $Pmnb$ and S.G. $Pmn2_1$) structures.[38–41] The XRD pattern of the 3LFS sample can be better refined with a $P2_1/n$ monoclinic structure. Therefore, Fe(III) in the raw material can be completely reduced to Fe(II) for forming $Li_{2-x}FeSi_{1-x}P_xO_4$/C in the synthetic process with 3–15% $NH_4H_2PO_4$. The addition of appropriate ratios of $NH_4H_2PO_4$ can inhibit impurity formation to obtain pure $Li_{2-x}FeSi_{1-x}P_xO_4$/C ($x = 0.03–0.15$). However, in the pattern of 0LFS, without $NH_4H_2PO_4$ in the synthesis process (Fig. 3), the peaks of the Fe_2O_3 impurity appear at $2\theta = 43°$ and $62°$, though the main diffraction peaks could be indexed as Li_2FeSiO_4. The appearance of the Fe_2O_3 impurity might be caused by the incomplete reduction of Fe(III) from the reaction source. When the $NH_4H_2PO_4$ amount was set to 1% ($x = 0.01$), the XRD pattern of the as-synthesized 1LFS shows the peaks of the impurity Li_4SiO_4; the other peaks accord with the ones of Li_2FeSiO_4. Additionally, when the

amount of introduced $NH_4H_2PO_4$ reached 20% ($x = 0.20$) during synthesis process, the obtained material 20LFS shows the obvious diffraction peak of Fe, illustrating that the introduced $NH_4H_2PO_4$ improves the reduction ability of the reactants too much so that a part of the Fe(III) is reduced to zerovalence Fe. This phenomenon is related to the strong reducibility of the system with $NH_4H_2PO_4$. On the basis of the aforementioned result, by adjusting the ratio of $NH_4H_2PO_4$ in the synthesis substances, the valence of Fe in the final products could be controlled to obtain pure $Li_{2-x}FeSi_{1-x}P_xO_4$/C ($x = 0.03–0.15$). In addition, no diffraction peaks of carbon could be found in any of the XRD patterns of the synthesized samples in Fig. 3 and S1,† which confirmed that the formed carbon in $Li_{2-x}FeSi_{1-x}P_xO_4$/C is amorphous.

The FTIR spectra of 0LFS, 1LFS, and 3LFS (Fig. 4a) have similar strong absorbance peaks at approximately 900 cm^{-1}, which is characteristic of the vibration of SiO_4^{4-},[3,34] and at 1500 cm^{-1}, which is attributed to the vibration of the carboxylic group[3] from the decomposition product of citric acid. The peak for PO_4^{3-} vibration, which should be at approximately 950 and 1050 cm^{-1} because of the symmetric stretching vibration mode of O–P–O in tetraphosphate compounds,[42] could not be observed and may have been covered by the strong vibrational peak of SiO_4^{4-}. The absorbance peaks of 1LFS are slightly different from those of the other materials and show a cluster of peaks at around 900 cm^{-1}. This result is possibly because of the existence of Li_4SiO_4, which confirms the results of the XRD analysis.

The Raman spectrum in Fig. 4b was obtained to study the structural properties of carbon in 3LFS. Two intense broad bands are found at 1332 and 1593 cm^{-1}, which are assigned to the D (disordered) band and the G (graphite) band of sp^2 type carbon in the samples, respectively. A lower D/G band intensity ratio indicates a higher electronic conductivity of the residual carbon. However, the D/G band intensity ratio is 0.889, which
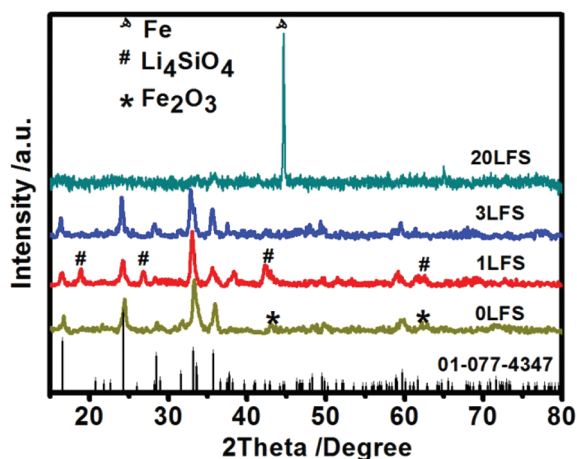

Fig. 3 XRD patterns of the as-synthesized 0LFS, 1LFS, 3LFS and 20LFS.
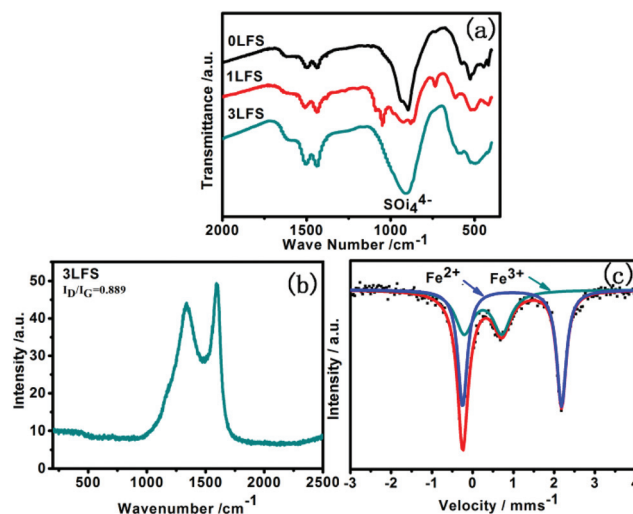

Fig. 4 FTIR spectra of samples 0LFS, 1LFS and 3LFS (a). Raman spectrum (b) and Mössbauer spectra (c) of sample 3LFS.

is not as low when compared with the results of other research groups,[43] indicating that the electronic conductivity is not as high. Moreover, an interesting phenomenon is observed, in which the peaks (550 and 900 cm^{-1}) assigned to the internal bending and stretching vibrations of the SiO_4^{4-} tetrahedra are not obvious, implying that the amorphous carbon coating on the 3LFS particles decreases the optical skin depth of the incident laser so that the penetration depth inside LFS is too short to be effective for data collection.[37]

The XPS spectra of 0LFS, 1LFS and 3LFS were measured and are displayed in Fig. S2.† The results show that the C 1s spectra consists of two peaks. The high intensity peak at 284.6 eV is attributed to the amorphous carbon present in the sample whereas a low intensity peak at 289.5 eV originates from some carboxylic groups.[3] Unfortunately, only the characteristics of Fe^{3+} (the binding energy peak positions for Fe 2p at 712.5 and 726 eV are assigned to 2p3/2 and 2p1/2, respectively) could be found, not those of Fe^{2+}, because the surface of the materials is entirely oxidized by atmospheric oxygen.[44–48] The Si 2p peak at 102.31 eV can be expected for SiO_2. The Li 1s peak at 55.4 eV represents the Li^+ in the materials whereas that centred at 56.9 eV can be attributed to Li_2CO_3.[45] The O 1s spectra of the original sample are composed of two peaks, the peak at higher binding energy (532.6 eV) originates from some carboxyl compounds. The very strong peak at 531.4 eV can be attributed to Li_2CO_3.[47,49] In addition, the content of different valence states of Fe in the as prepared 3LFS ($x = 0.03$) was confirmed from the Mössbauer spectra. The Mössbauer spectra are shown in Fig. 4c and fitted as being composed of two doublets.[50] One of the doublets originates from the Fe^{2+}, which is the same as Dragana Jugović's result,[51] and the other from the superficial Fe^{3+} oxidised from the Fe^{2+} phase in the process of storage for a long time before the Mössbauer spectra of the sample was measured. The result shows that the atom rate of Fe^{2+} and Fe^{3+} is 4 : 6 indicating that the Fe^{2+} is easily oxidised to Fe^{3+} in the synthesized sample. Moreover, an ICP test of Li and Fe was performed using the same sample that was used to measure the Mössbauer spectra. The result shows that the concentrations of Fe and Li are 23.83 and 6.022 mg L^{-1}, respectively. The calculated atomic ratio is about 1 : 2.02, which is extremely close to 1 : 2, indicating that there should be mainly Fe^{2+} in the new-synthesized sample. In the oxidation process, Fe^{2+} change to Fe^{3+} on the surface of the sample, while the Li^+ translated into Li_2CO_3 or other lithium salt, which is also certified by the results of XPS.

The schematic illustration for the formation of $Li_{2-x}FeSi_{1-x}P_xO_4/C$ including the processes A1, A2, and A3, is presented in Scheme 1. First, a gel was obtained, which includes nano-sized SiO_2 that was uniformly mixed with the Fe(III) compound $Fe(NO_3)_3 \cdot 9H_2O$, $LiCH_3COOH \cdot 2H_2O$, citric acid, and $NH_4H_2PO_4$ in a solvent, and then treated at 70 °C until the formation of a dry gel. The final $Li_{2-x}FeSi_{1-x}P_xO_4/C$ materials were coated with carbon by ball-milling the obtained dry gel with sucrose (A2) and calcining under the atmosphere of Ar (A3). Here, the process A3 in the synthetic procedure is complex, which can be written as eqn (A3), but it's important

to understanding the detailed reactions for the aim of obtaining $Li_{2-x}FeSi_{1-x}P_xO_4/C$.

According to the results of the XRD, the mechanism of this system with $NH_4H_2PO_4$ might be as follows: here, the introduced $NH_4H_2PO_4$ decomposes to H_3PO_4 and NH_3 when the temperature is about 210 °C.[52] The amount of produced NH_3 is small so that it could adsorb on the surface of the material particles and/or fill in the porosity in the large pores for a period of time. When the temperature reaches 550–650 °C, the as-produced NH_3 can give H_2 (eqn (A3-1))[53] providing a reducing environment in every particle of the reactants, guaranteeing a complete change from Fe^{3+} to Fe^{2+}. Compared with the H_2 atmosphere from the outside of the block of the reactants, the needed amount of H_2 produced by this system itself should be very small and the security is higher obviously. However, it's difficult to decompose NH_3 to produce H_2 without a catalyst (eqn (A3-1)). Fortunately, in this synthetic system, the reactants of $Fe(NO_3)_3$ and sucrose could change to Fe_2O_3/C in the heating process (eqn (A3-2)). As the intermediate for synthesizing the final $Li_{2-x}FeSi_{1-x}P_xO_4/C$, Fe_2O_3/C can act as the catalyst for the decomposition reaction from NH_3 to H_2 (eqn (A3-1)). However, if there is too much $NH_4H_2PO_4$, the decomposed abundant H_2 could cause the intermediate Fe_2O_3 to be reduced to Fe (eqn (A3-3)).[54,55]

To confirm this mechanism, as an example, the gas produced in the process of calcination between 350–650 °C with the molar ratio of $n(NH_4H_2PO_4)/n(NH_4H_2PO_4 + SiO_2) = 20\%$ was collected and analyzed through gas chromatography. To compare, the gas chromatography of pure H_2, pure Ar, and ixed gas $(V_{H_2} : V_{Ar} = 1 : 4)$ were measured at the same conditions. The results are shown in Fig. 5. It can be seen that the H_2 existed. The retention time of pure H_2 and pure Ar was 0.57 and 0.66 min, respectively. While, in the mixed gas $(V_{H_2} : V_{Ar} = 1 : 4)$, the retention time of H_2 and Ar was 0.54 and 0.66 min, respectively. The retention time of H_2 of the mixed gas $(V_{H_2} : V_{Ar} = 1 : 4)$ is shifted a little compared with that of pure H_2. The retention time of the peak of the collected gas at 0.54 min is the same as that of H_2 in the mixed gas
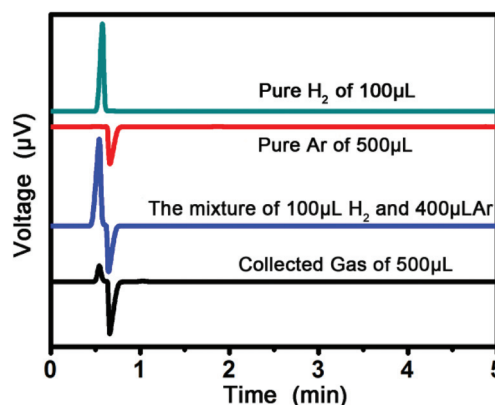

Fig. 5 Gas chromatography of pure H_2 (green), pure Ar (red), mixed gas $(V_{H_2} : V_{Ar} = 1 : 4)$ (blue) and the collected gas produced in the reaction process of 20LFS (black).

$(V_{H_2} : V_{Ar} = 1 : 4)$. Also, the retention time of the peak of the collected gas at 0.66 min is almost the same as that of Ar in the mixed gas $(V_{H_2} : V_{Ar} = 1 : 4)$. These results verified the formation of H_2 that mixed into the Ar in the experiment process.

The charge–discharge properties of the as-synthesized materials 0LFS, 1LFS, and 3LFS were determined, and the obtained curves are displayed in Fig. 6(a–c). In the charging processes, all of the materials in the first cycle possess a high voltage plateau (approximately 4.5 V), which might be caused by structural rearrangement involving the exchange of lithium and iron between their sites.[17,35] The high charge voltage profile in the initial charge at room temperature was also reported by Titus Masese et al.[26] The charge curves of 1LFS and 3LFS are stable at around 3.0 and 2.9 V in the next cycles, whereas the charge curve of 0LFS needs one more cycle to reach the stable state. This observation should be attributed to the appearance of the Fe_2O_3 impurity, which might participate in the electrochemical reaction.[56]

The curves of discharge processes are considerably different from that of charge processes. The discharge curves of 1LFS and 3 LFS are almost similar, with a platform at around 2.6 V in all cycles, implying high cycling stability. By comparison, 0LFS displays a trend in which the discharge plateaus gradually increase from 2.3 V in the first cycle to 2.8 V in the 20th cycle, which might be caused by the Fe_2O_3 impurity.[57,58] 3LFS exhibits an initial discharge capacity of approximately 179 mA h g^{-1}, corresponding to more than one lithium insertion per formula unit, excluding the decomposition of electrolyte.[15] This result is consistent with the coulombic efficiency of 3LFS. However, the first specific discharge capacities of 0LFS and 1LFS are 164 and 115 mA h g^{-1}, respectively. The numbers of Li–ion extraction/insertion for 0LFS and 1LFS are difficult to confirm because of the presence of impurities. In this study,

the lower discharge capacities of 0LFS and 1LFS may be caused by the presence of Fe_2O_3 and Li_4SiO_4 impurities, respectively. However, Fe_2O_3 can exhibit electrochemical activity, which would increase the discharge capacity, though its contribution would be mainly in the low charge–discharge potential window. On the other hand, given that Fe_2O_3 possesses electric conductivity and Li_4SiO_4 is an insulator,[36] the first-cycle specific discharge capacity of 1LFS is higher than that of 0LFS, which is identical to the reported high capacity of Li_2FeSiO_4 that is mainly due to superb electrical conductibility.

This observation is supported by the EIS results of the as-synthesized materials (Fig. 6h). The radius of the high-frequency semicircle of EIS atlas is related to the contact impedance between the electrode material and the electrolyte in the charge transfer process. The slope of the low-frequency straight line is associated with Warburg impedance of the lithium ion diffusion in the electrode material. The EIS results evidently demonstrate that the charge transfer resistance of Li^+ through the 1LFS cathode is significantly higher than those of the 0LFS and 3LFS cathodes. This difference should be caused by the presence of the nonconductive Li_4SiO_4 impurity in 1LFS, thus increasing the impedance. The charge transfer resistance of Li^+ through 0LFS is the smallest because the impurity Fe_2O_3 can show high electronic conductivity when coated with carbon,[36] which reduces impedance.

Fig. 6(d–f) show the CV curves of the first two cycles of the as-synthesized composites 0LFS, 1LFS and 3LFS. The first-cycle CV curves of all of the samples are similar. The anodic peak of 0LFS appears at 3.5 V, whereas those of 1LFS and 3LFS locate at around 3.3 V. The cathodic peaks all occur at approximately 2.5 V, which corresponds to the Fe^{2+}/Fe^{3+} redox couple. In the second cycle, the potential values of the anodic peaks of 0LFS, 1LFS, and 3LFS are 3.30, 3.16, and 3.07 V, respectively, which are smaller than those in the first cycle. The higher anodic peak potential of 0LFS agrees well with its higher charge platform in Fig. 6a. Furthermore, when the potential values reach approximately 4.3 V in the potential positive scanning, the small peak might be caused by the decomposition of electrolyte.[15] Meanwhile, the cathodic peaks of the samples have no split. This finding demonstrates that one Li^+ is extracted, which is consistent with the charge–discharge result of the as-synthesized materials. Moreover, the peak potential separations of 0LFS, 1LFS, and 3LFS are 800, 660, and 570 mV, respectively, in the second cycle. 3LFS shows a smaller peak separation potential, suggesting the lowest electrochemical polarization and enhanced electrochemical reversibility of the Li insertion or extraction processes; thus, 3LFS has a relatively high discharge capacity. However, the carbon coating is not uniform enough and particle agglomeration clearly occurs, resulting in the not-so high discharge capacities of the synthesized materials. Investigation of this system, with more effective conductivity net, is being conducted.

The cycling stability of the as-synthesized materials (Fig. 6g) show that the capacity degradation of these materials mainly occurs in the first five cycles. The discharge capacities of 0LFS, 1LFS, and 3LFS after five cycles were reduced by approximately
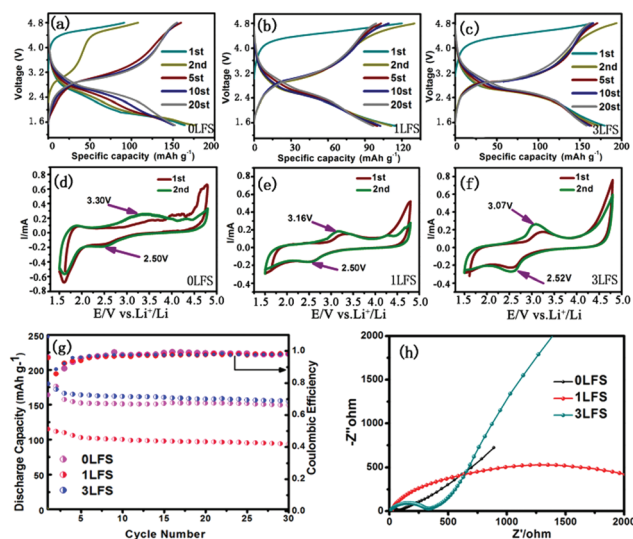

Fig. 6 Charge–discharge curves for the 1st, 2nd, 5th, 10th, and 20th cycles (a, b and c), CV curves for the 1st and 2nd cycles (d, e and f), cycle performance and coulombic efficiency (g) and EIS (h) for the $Li_{2-x}FeSi_{1-x}P_xO_4$/C materials 0LFS, 1LFS and 3LFS.

6.7%, 10.4%, and 8.9%, respectively, relative to their first cycle discharge capacities. After five cycles, their specific discharge capacities are more stable. The discharge capacity retentions of 0LFS, 1LFS, and 3LFS, after 30 cycles are approximately 98.7%, 91.9%, and 94.5% of their corresponding discharge capacities in the sixth cycle. Moreover, the coulombic efficiencies of 0LFS, 1LFS, and 3LFS remain at 98.0%, 98.1% and 97.8% after 30 cycles, respectively, which suggests reliable redox reversibility.

Conclusions

In this study, pure $Li_{2-x}FeSi_{1-x}P_xO_4/C$ ($x = 0.03–0.15$) materials were prepared by using the low cost compound Fe-$(NO_3)_3 \cdot 9H_2O$, with the help of citric acid and appropriate ratios of $NH_4H_2PO_4$ in the synthesis procedure. The mechanism analysis of the system shows that there is a catalysis process, which helps to produce H_2, providing a reducing environment in every particle of the reactants. This guarantees the complete change from Fe^{3+} to Fe^{2+}. Moreover, the ratios of $NH_4H_2PO_4$ used in this system could adjust the valence of the element Fe in the products. Without $NH_4H_2PO_4$, an Fe_2O_3 impurity is formed accompanying the Li_2FeSiO_4. With the addition of 1 at% $NH_4H_2PO_4$, the Li_4SiO_4 impurity accords with the objective $Li_{2-x}FeSi_{1-x}P_xO_4/C$. By adjusting $NH_4H_2PO_4$ to 3–15 at%, the valence of Fe in the obtained sample was completely controlled as Fe(II), which guarantees the purity of $Li_{2-x}FeSi_{1-x}P_xO_4/C$. Meanwhile, Fe with zero-valence could be found as an impurity with the addition of 20 at% $NH_4H_2PO_4$ due to overreduction in the system. The electrochemical measure confirmed that the pure $Li_{2-x}FeSi_{1-x}P_xO_4/C$ ($x = 0.03$) displayed the highest discharge capacity of 179 mA h g^{-1}, in the first cycle and the best discharge capacity retention of 98.7% after 30 cycles comparing to their corresponding discharge capacities in the sixth cycle. Moreover, its reliable redox reversibility is confirmed by the coulombic efficiencies.

Acknowledgements

References

1 Z. L. Gong and Y. Yang, *Energy Environ. Sci.*, 2011, **4**, 3223–3242.

2 J. B. Goodenough and K. S. Park, *J. Am. Chem. Soc.*, 2013, **135**, 1167–1176.

3 S. Singh and S. Mitra, *Electrochim. Acta*, 2014, **123**, 378–386.

4 M. Ebner, F. Marone, M. Stampanoni and V. Wood, *Science*, 2013, **342**, 716–720.

5 J. Lee, A. Urban, X. Li, D. Su, G. Hautier and G. Ceder, *Science*, 2014, **343**, 519–522.

6 B. L. Ellis, K. T. Lee and L. F. Nazar, *Chem. Mater.*, 2010, **22**, 691–714.

7 J. B. Goodenough and Y. Kim, *Chem. Mater.*, 2010, **22**, 587–603.

8 Q. Cao, H. P. Zhang and G. J. Wang, *Electrochem. Commun.*, 2007, **9**, 1228–1232.

9 W. H. Chen, J. J. Zhao, Y. Y. Li, S. Li, C. C. Jin, C. C. Yang, X. M. Feng, J. M. Zhang and L. W. Mi, *ChemElectroChem*, 2014, **1**, 601–610.

10 T.-H. Tran, S. Harmand, B. Desmet and F. Pailhoux, *J. Electrochem. Soc.*, 2013, **160**, A775–A780.

11 K. Amine, Z. Chen, Z. Zhang, J. Liu, W. Lu, Y. Qin, J. Lu, L. Curtis and Y. Sun, *J. Mater. Chem.*, 2011, **21**, 17754–17759.

12 Y. H. Huang and J. B. Goodenough, *Chem. Mater.*, 2008, **20**, 7237–7241.

13 T. Muraliganth, K. R. Stroukoff and A. Manthiram, *Chem. Mater.*, 2010, **22**, 5754–5761.

14 W. H. Chen, M. Lan, D. Zhu, C. C. Jin, X. M. Feng, C. C. Yang, J. M. Zhang and L. W. Mi, *J. Mater. Chem. A*, 2013, **1**, 10912–10917.

15 W. H. Chen, M. Lan, D. Zhu, C. L. Wang, S. R. Xue, C. C. Yang, Z. X. Li, J. M. Zhang and L. W. Mi, *RSC Adv.*, 2013, **3**, 408–412.

16 M. K. Devaraju, T. Tomai and I. Honma, *Electrochim. Acta*, 2013, **109**, 75–81.

17 A. Nytén, A. Abouimrane, M. Armand, T. Gustafsson and J. O. Thomas, *Electrochem. Commun.*, 2005, **7**, 156–160.

18 X. Z. Wu, X. Jiang, Q. S. Huo and Y. X. Zhang, *Electrochim. Acta*, 2012, **80**, 50–55.

19 H. Y. Gao, Z. Hu, K. Zhang, F. Y. Cheng and J. Chen, *Chem. Commun.*, 2013, **49**, 3040–3042.

20 M. Li, L. L. Zhang, X. L. Yang, H. B. Sun, Y. H. Huang, G. Liang, S. B. Ni and H. C. Tao, *RSC Adv.*, 2015, **5**, 22818–22824.

21 R. Dominko, M. Bele, M. Gaberšček, A. Meden, M. Remškar and J. Jamnik, *Electrochem. Commun.*, 2006, **8**, 217–222.

22 T. Muraliganth, K. R. Stroukoff and A. Manthiram, *Chem. Mater.*, 2010, **22**, 5754–5761.

23 Z. X. Chen, S. Qiu, Y. L. Cao, J. F. Qian, X. P. Ai, K. Xie, X. B. Hong and H. X. Yang, *J. Mater. Chem. A*, 2013, **1**, 4988–4992.

24 H. Zhu, X. Z. Wu, L. Zan and Y. X. Zhang, *Electrochim. Acta*, 2014, **117**, 34–40.

25 D. P. Lv, W. Wen, X. K. Huang, J. Y. Bai, J. X. Mi, S. Q. Wu and Y. Yang, *J. Mater. Chem.*, 2011, **21**, 9506–9512.

26 T. Masese, Y. Orikasa, C. Tassel, J. Kim, T. Minato, H. Arai, T. Mori, K. Yamamoto, Y. Kobayashi, H. Kageyama, Z. Ogumi and Y. Uchimoto, *Chem. Mater.*, 2014, **26**, 1380–1384.

27 D. P. Lv, J. Y. Bai, P. Zhang, S. Q. Wu, Y. X. Li, W. Wen, J. Zheng, J. X. Mi, Z. Z. Zhu and Y. Yang, *Chem. Mater.*, 2013, **25**, 2014–2020.

28 A. R. Armstrong, N. Kuganathan, M. S. Islam and P. G. Bruce, *J. Am. Chem. Soc.*, 2011, **133**, 13031–13035.

29 J. Yi, M. Y. Hou, H. L. Bao, C. X. Wang, J. Q. Wang and Y. Y. Xia, *Electrochim. Acta*, 2014, **133**, 564–569.

30 T. Masese, Y. Orikasa, T. Mori, K. Yamamoto, T. Ina, T. Minato, K. Nakanishi, T. Ohta, C. Tassel, Y. Kobayashi, H. Kageyama, H. Arai, Z. Ogumi and Y. Uchimoto, *Solid State Ionics*, 2014, **262**, 110–114.

31 J. F. Cui, C. X. Qing, Q. T. Zhang, C. Su, X. M. Wang, B. P. Yang and X. B. Huang, *Ionics*, 2014, **20**, 23–28.

32 J. L. Yang, X. C. Kang, D. P. He, T. Peng, L. Hu and S. C. Mu, *J. Power Sources*, 2013, **242**, 171–178.

33 K. I. Onlamee, B. Sunisa, K. Wantana, L. Wanwisa, S. Sutham and M. Nonglak, *Int. J. Electrochim. Sci.*, 2014, **9**, 4257–4267.

34 X. M. Wang, C. X. Qing, Q. T. Zhang, W. F. Fan, X. B. Huang, B. P. Yang and J. F. Cui, *Electrochim. Acta*, 2014, **134**, 371–376.

35 K. Gao, J. Zhang and S. D. Li, *Mater. Chem. Phys.*, 2013, **139**, 550–556.

36 H. T. Zhou, M.-A. Einarsrud and F. Vullum-Bruer, *J. Power Sources*, 2013, **235**, 234–242.

37 L. L. Zhang, S. Duan, X. L. Yang, G. Peng, G. Liang, Y. H. Huang, Y. Jiang, S. B. Ni and M. Li, *ACS Appl. Mater. Interfaces*, 2013, **5**, 12304–12309.

38 S. Nishimura, S. Hayase, R. Kanno, M. Yashima, N. Nakayama and A. Yamada, *J. Am. Chem. Soc.*, 2008, **130**, 13212–13213.

39 C. Sirisopanaporn, A. Boulineau, D. Hanzel, R. Dominko, B. Budic, A. Robert Armstrong, P. G. Bruce and C. Masquelier, *Inorg. Chem.*, 2010, **49**, 7446–7451.

40 G. Mali, C. Sirisopanaporn, C. Masquelier, D. Hanzel and R. Dominko, *Chem. Mater.*, 2011, **23**, 2735–2744.

41 J. L. Yang, X. C. Kang, L. Hu, X. Gong, D. P. He, T. Peng and S. C. Mu, *J. Alloys Compd.*, 2013, **572**, 158–162.

42 W. Kim, W. Ryu, D. Han, S. Lim, J. Eom and H. Kwon, *ACS Appl. Mater. Interfaces*, 2014, **6**, 4731–4736.

43 Z. M. Zheng, Y. Wang, A. Zhang, T. R. Zhang, F. Y. Cheng, Z. L. Tao and J. Chen, *J. Power Sources*, 2012, **198**, 229–235.

44 S. Zhang, C. Deng, B. L. Fu, S. Y. Yang and L. Ma, *Electrochim. Acta*, 2010, **55**, 8482–8489.

45 D. Ensling, M. Stjerndahl, A. Nytén, T. Gustafsson and J. O. Thomas, *J. Mater. Chem.*, 2009, **19**, 82–88.

46 A. Nytén, M. Stjerndahl, H. Rensmo, H. Siegbahn, M. Armand, T. Gustafsson, K. Edstrom and J. O. Thomas, *J. Mater. Chem.*, 2006, **16**, 3483–3488.

47 C. Deng, S. Zhang, Y. Gao, B. Wu, L. Ma, Y. H. Sun, B. L. Fu, Q. Wu and F. L. Liu, *Electrochim. Acta*, 2011, **56**, 7327–7333.

48 L. Castro, R. Dedryvère, M. Khalifi, P. E. Lippens, J. Bréger, C. Tessier and D. Gonbeau, *J. Phys. Chem. C*, 2010, **114**, 17995–18000.

49 Y. Xu, Y. J. Li, S. Q. Liu, H. L. Li and Y. N. Liu, *J. Power Sources*, 2012, **220**, 103–107.

50 R. Y. Chen, R. Heinzmann, S. Mangold, V. S. K. Chakravadhanula, H. Hahn and S. Indris, *J. Phys. Chem. C*, 2013, **117**, 884–893.

51 D. Jugović, M. Milović, V. N. Ivanovski, M. Avdeev, R. Dominko, B. Jokić and D. Uskoković, *J. Power Sources*, 2014, **265**, 75–80.

52 W. W. Wu, X. H. Wu, S. B. Lai, Y. J. Fan and S. Liao, *Trans. Nonferrous Met. Soc. China*, 2008, **60**, 84–87.

53 W. J. Yang, N. Y. Tao, F. L. Liu, Z. Y. Li and C. C. Guo, *Journal of Hunan University (Natural Sciences)*, 2006, **33**, 100–104.

54 P. Pourghahramani and E. Forssberg, *Thermochim. Acta*, 2007, **454**, 69–77.

55 V. I. Zenkov and V. V. Pasichnyi, *Powder Metall. Met. Ceram.*, 2010, **49**, 231–237.

56 J. S. Cho, Y. J. Hong and Y. C. Kang, *ACS Nano*, 2015, **9**, 4026–4035.

57 M. V. Reddy, T. Yu, C.-H. Sow, Z. X. Shen, C. T. Lim, G. V. Subba Rao and B. V. R. Chowdari, *Adv. Funct. Mater.*, 2007, **17**, 2792–2799.

58 W. Xiao, Z. X. Wang, H. J. Guo, Y. H. Zhang, Q. Zhang and L. Gan, *J. Alloys Compd.*, 2013, **560**, 208–214.